Crystallization of chiral active Brownian particles at low densities

Kangeun Jeong [1,*] Yuta Kuroda [1] Yuki Asatani,[1] Takeshi Kawasaki [2,3] and Kunimasa Miyazaki [1,†]
[1]Department of Physics, Nagoya University, Nagoya 464-8602, Japan
[2]D3 Center, The University of Osaka, Toyonaka, Osaka 560-0043, Japan
[3]Department of Physics, The University of Osaka, Toyonaka, Osaka 560-0043, Japan

(Received 14 July 2025; accepted 12 October 2025; published 24 November 2025)

Chiral active matter is a variant of active matter systems in which the motion of the constituent particles violates mirror symmetry. In this article, we simulate two-dimensional chiral Active Brownian Particles, the simplest chiral model in which each particle undergoes circular motion, and show that the system crystallizes at low densities well below the melting point of the equilibrium counterpart. Crystallization is only possible if the orbital radius is long enough to align the circulating particles, but short enough for neighboring particles to avoid collisions. Of course, the system must be driven sufficiently far from equilibrium, since chirality cannot affect thermodynamic properties in classical equilibrium systems. The fluid-crystal phase diagram shows a re-entrant melting transition as a function of the radius of the circles. We show that at least one of the two transitions follows the same two-step melting scenario as in equilibrium systems.

DOI: 10.1103/yntx-ss9r

I. INTRODUCTION

The macroscopic properties of classical systems in equilibrium are known to be unaffected by chirality (or broken mirror symmetry) in the underlying microscopic equations of motion [1,2]. For example, a magnetic field that induces chiral motion of point charges cannot induce macroscopic magnetization, according to the Bohr-van Leeuwen theorem [3,4]. This is not the case when the system is taken out of equilibrium, where it is expected that the interplay of chirality and violation of detailed balance will lead to phenomena not found in equilibrium systems. Active matter, due to its intrinsic nonequilibrium nature, offers an ideal test bed for studying such phenomena [5]. Chiral motions are abundant in biological systems. Many living systems, such as bacteria, cells, and algae, perform circular and spinning motions [6–8]. Chiral active matter systems can also be easily designed and realized using synthetic particles, such as asymmetric colloidal particles and Quincke rollers [9,10]. Over the past decade, studies on chiral active matter have revealed rich collective behaviors not observed in nonchiral systems. These include vortex formation in flocking systems [10], nonreciprocal transport [11], and even the crystallization of spinning particles [12–15]. However, the microscopic mechanisms underlying these exotic phenomena remain largely elusive. In particular, it is desirable to understand how the chirality of the microscopic equations affects the fluid-solid phase transition and the glass (or jamming) transitions [16,17].

In this article, we focus on the crystallization of a chiral active matter model consisting of circularly orbiting particles. To this end, we use the simplest model of this kind, chiral Active Brownian Particles (cABP). The cABP model is a chiral variant of the ABP model [18]. The equation of motion of the ith cABP is assumed to be governed by an overdamped Langevin equation:

$$\dot{\boldsymbol{r}}_i = -\frac{1}{\zeta}\frac{\partial U}{\partial \boldsymbol{r}_i} + v_0 \hat{\boldsymbol{e}}_i, \tag{1}$$

where ζ is the drag coefficient and U is the interaction potential. $\hat{\boldsymbol{e}}_i$ is the orientation of the self-propulsion force, which satisfies

$$\dot{\hat{\boldsymbol{e}}}_i = \left(\Omega\hat{\boldsymbol{z}} + \sqrt{\frac{2}{\tau_p}}\,\boldsymbol{\eta}_i\right) \times \hat{\boldsymbol{e}}_i. \tag{2}$$

Here, $\boldsymbol{\eta}_i$ represents Gaussian white noise with zero mean, which satisfies $\langle \eta_{i,\alpha}(t)\eta_{j,\beta}(t')\rangle = \delta_{ij}\delta_{\alpha\beta}\delta(t-t')$, where α and β represent the coordinates. v_0 and τ_p denote the noise strength and its persistence time, respectively. Ω is the angular frequency with respect to the rotation axis $\hat{\boldsymbol{z}}$ that causes the particles to move in a circular motion with a radius $R = v_0/\Omega$. The two key parameters of the model are τ_p, which controls the distance from equilibrium, and R, which characterizes the extent of chiral motion. When τ_p is very small, the fluctuation-dissipation theorem is recovered, and thus the equation becomes that of equilibrium Brownian motion, even when Ω is finite. Recently, the two-dimensional system in the large τ_p limit has been studied extensively at low densities by Lei *et al.* [19]. They discovered that the system undergoes an absorbing phase transition from a diffusive ergodic state to a quiescent nonergodic state. The most striking feature of cABP in the absence of stochastic noise ($\tau_p = \infty$) is hyperuniformity (HU): strong suppression of density fluctuations over long length scales [20]. According to Ref. [19], HU has been observed not only in the vicinity of the absorbing

*Contact author: jeong@r.phys.nagoya-u.ac.jp
†Contact author: miyazaki@r.phys.nagoya-u.ac.jp

phase transition [21], but also throughout an entire active phase. Kuroda *et al.* have investigated the fate of this two-dimensional noiseless cABP at high densities and found that the system crystallizes [22]. Surprisingly, this crystalline state is characterized by true long-range translational order, which is strictly forbidden in equilibrium systems in two dimensions by the Mermin-Wagner theorem [23]. The authors of Ref. [22] argued that the HU of cABP is responsible for the ultrastability of the crystalline phase. This stability persists as long as $\Omega \neq 0$, where HU survives. However, this argument applies only for the noiseless limit, i.e., $\tau_p = \infty$.

Here, we consider the case in which τ_p is finite and the density is relatively low. We numerically simulate the cABP system for a wide range of Ω, τ_p, and densities. We find that the system crystallizes at densities well below the melting point of equilibrium two-dimensional systems. The mechanism of crystal formation is deceptively simple. The particles undergo circular motion with a radius $R = v_0/\Omega$, which increases their effective radius. This reduces the available free volume and promotes crystallization. Crystallization occurs when the effective packing fraction defined by the effective radius becomes sufficiently high. However, if R becomes too large, strong collisions between particles distort their circular orbits, render their trajectories chaotic, and eventually destroy the crystalline structure. The persistence time τ_p should also be within the appropriate range. If τ_p is infinitesimally small, the noise in Eq. (1) becomes Markovian, detailed balance is restored, and thus chirality cannot induce crystallization even when R is finite. When τ_p is infinite, the noise in Eq. (2) disappears, and thus the system enters an absorbing state, in which each particle resides at a fixed point without interacting [19]. The crystal that we observe showcases order by disorder, as finite noise is essential [24]. Additionally, we found that crystallization follows the two-step melting transition scenario as in the Kosterlitz-Thouless-Halperin-Nelson-Young (KTHNY) theory [25].

II. METHOD

We simulate one-component cABP systems in two dimensions by solving Eqs. (1) and (2). For the interparticle potential $U = \sum_{i>j} \phi(r_{ij})$, where r_{ij} is the distance between the ith and jth particles, we use the Weeks-Chandler-Andersen potential:

$$\phi(r) = 4\epsilon\left\{\left(\frac{\sigma}{r}\right)^{12} - \left(\frac{\sigma}{r}\right)^{6} + \frac{1}{4}\right\}\Theta(2^{1/6}\sigma - r), \quad (3)$$

where σ is the particle diameter and $\Theta(x)$ is the Heaviside step function. The interaction potential has a cutoff length of $2^{1/6}\sigma$, resulting in purely repulsive forces between particles. We choose σ and σ/v_0 as units of length and time, respectively. The energy ratio $\epsilon/v_0\zeta\sigma$ is set to 1/24 [19]. The important control parameters in the present study are the orbital radius $R = v_0/\Omega$, the persistence time τ_p, and the density (or packing fraction) $\varphi = N\pi\sigma^2/(4L_xL_y)$, where N is the total number of particles, and L_x and L_y are the side lengths of the simulation box.

To accommodate the hexagonal lattice under periodic boundary conditions, the simulation box is usually designed with an aspect ratio of $L_x{:}L_y = 7{:}4\sqrt{3}$ [22]. Most simulations

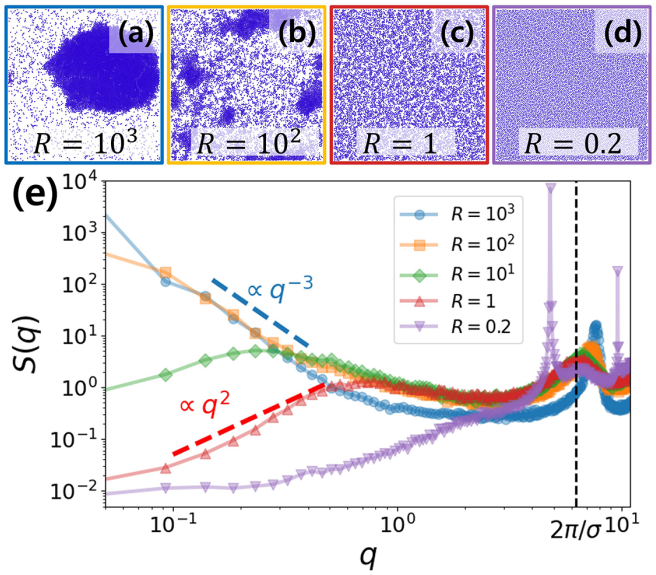

FIG. 1. (a)–(d) Snapshots of the stationary state of cABP for various values of $R = v_0/\Omega$ at $\varphi = 0.4$, $v_0 = 1$, and $\tau_p = 200$. (a) $R = 10^3$, (b) 10^2, (c) 1, and (d) 0.2. (e) $S(\boldsymbol{q})$ for several R values. The thick two broken lines indicate q^{-3} and q^2. The thin vertical line shows the position of $q = 2\pi/\sigma$. The system size is $N = 10^4$.

are carried out for the system size of $N = 9464$. Larger systems of $N = 40\,824$ are used to compute correlation functions with high precision near the transition point. Further details of the simulation setup can be found in the Supplemental Material [26].

Unless otherwise stated, the packing fraction is set to $\varphi = 0.4$. This value is much smaller than the melting point for the equilibrium hard discs $\varphi \approx 0.7$ at which the system undergoes the hexatic-solid transition [27]. Throughout this work, v_0 is fixed to unity. The results remain qualitatively unchanged for other values of v_0 [19]. We first choose $\tau_p = 200$, for which the Péclet number defined by $\mathrm{Pe} = \tau_p v_0/\sigma$ is sufficiently large to induce motility-induced phase separation (MIPS) when $R = \infty$ (or $\Omega = 0$) [28].

III. RESULTS

Figures 1(a)–1(d) show snapshots of particle configurations for several values of R. As expected, the system undergoes MIPS and forms large clusters of densely packed regions when R is large. As R decreases, the clusters become smaller and the boundary of the phase-separated region becomes blurred [19]. At $R = 0.2$, the system becomes spatially homogeneous. Figure 1(e) shows the static structure factor defined by $S(\boldsymbol{q}) = \langle|\delta\rho_{\boldsymbol{q}}|^2\rangle/N$, where $\delta\rho_{\boldsymbol{q}}$ is the Fourier-transformed density fluctuation at wave vector $\boldsymbol{q}$. At $R = 10^3$, where MIPS is clearly visible, $S(\boldsymbol{q})$ diverges as q^{-3} at small q, as predicted by Porod's law as a signature of phase separation [29,30]. As R decreases below $R \approx 10^2$, $S(\boldsymbol{q})$ at small q decreases and exhibits power-law behavior $S(\boldsymbol{q}) \sim q^{\alpha}$ with a positive exponent α. This is a clear sign of hyperuniformity [19,20]. Density fluctuations are suppressed because neighboring particles constrain particle trajectories, which facilitates the dissolution of large clusters. This is consistent

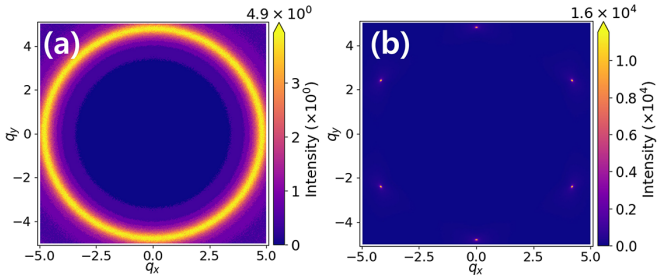

FIG. 2. The heat map of the structure factor $S(\boldsymbol{q})$ for $\varphi = 0.4$ and $\tau_p = 10^2$ at (a) $R = 0.299$ and (b) $R = 0.294$. The color sidebar shows the intensity of the $S(\boldsymbol{q})$.

with the disappearance of MIPS observed in Figs. 1(a)–1(d). It is theoretically established that the HU exponent $\alpha = 2$ in the large τ_p limit [19,31]. HU behavior is observed around $R = 1$–10, though this algebraic behavior tapers off at small q. The crossover from HU to a constant $S(\boldsymbol{q})$ occurs when τ_p is finite [19]. Concomitantly, the first peak of $S(\boldsymbol{q})$ initially found around $q = 2\pi/\sigma$ shifts to lower q and the width of the peak widens. This reflects the fact that the tightly packed particles in the MIPS clusters dissolve into a homogeneous fluid. As R decreases below 2, the MIPS clusters completely disappear and the system becomes homogeneous. The height of $S(\boldsymbol{q})$ at small q decreases and the HU behavior of $S(\boldsymbol{q}) \sim q^2$ fades out. Surprisingly, at the smallest R value of 0.2, the first peak suddenly sharpens and its height increases. This indicates the formation of crystals. Figure 2 shows the two-dimensional contour plot of $S(\boldsymbol{q})$ below and above the transition at which the sharp peak appears. The emergence of crystalline order with sixfold symmetry is clearly visible. Figure 3 shows the instantaneous configurations of the particles, which are colored according to the local hexatic order parameter $|\psi_6^i|$ (see definition below). At first glance, crystalline order is not apparent in the configurations of the particles. They appear completely random. However, the crystalline order becomes clearly visible when the trajectories of particles are superimposed, as shown in the inset of Fig. 3(a) (see also the movies available in the Supplemental Material [26]). The order becomes even more evident when one plots the positions of the centers of circular orbits, defined as $\boldsymbol{r}_i^0 \equiv \boldsymbol{r}_i - R\hat{\boldsymbol{z}} \times \hat{\boldsymbol{e}}_i$, as

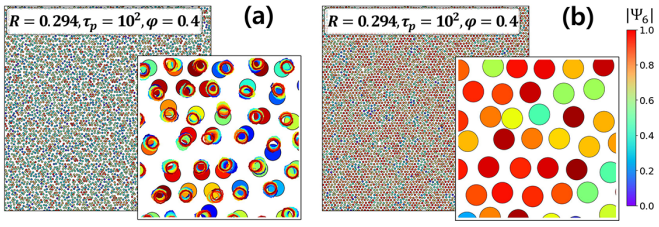

FIG. 3. (a) Snapshot of the particle configuration at $R = 0.294$, $\tau_p = 10^2$, and $\varphi = 0.4$. The color of each particle represents the magnitude of its local hexatic order parameter $|\psi_6^i|$ (see the color bar). The inset shows a magnified view with particle trajectories superimposed to highlight their circular motion. (b) The configuration of the centers of mass of the orbits for the configuration in panel (a). The size of the circles representing the center positions is identical to that of the particles.

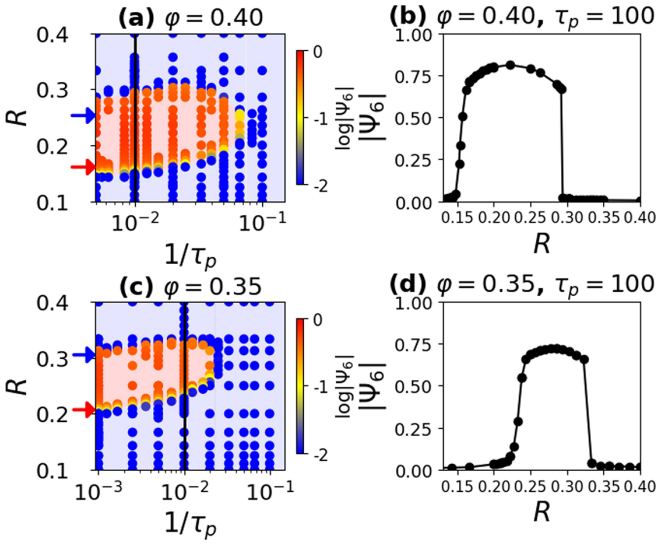

FIG. 4. (a) Phase diagram at $\varphi = 0.4$. The color of the dots represents $|\Psi_6|$. Blue and red arrows indicate the upper and lower phase boundaries, respectively, as estimated from a geometric argument (see text). (b) The dependence of $|\Psi_6|$ on R at $\tau_p = 10^2$ [shown as the solid line in panel (a)]. Panels (c) and (d) present the same plots for $\varphi = 0.35$.

demonstrated in Fig. 3(b). Larger value of $|\psi_6^i|$ indicates the emergence of hexatic order. In retrospect, the formation of the crystal is not surprising. A particle circulates with a radius R and behaves like a larger particle with an effective radius $R_{\text{eff}} = R + \sigma/2$, allowing the crystal to form at small packing fractions, similar to a vortex lattice in superconductors [32]. One would expect crystallization to occur when R_{eff} is small enough that all orbiting particles can be embedded in a hexatic lattice. At the same time, R must be large enough so that the particles do not melt into a fluid phase at low densities. Additionally, τ_p needs to be reasonably large for the crystal to form. Recall that, in the limit of $\tau_p \to 0$, the ABP model reduces to an equilibrium Brownian particle system that is in a fluid phase at $\varphi = 0.4$. Turning on Ω cannot change the phase diagram of the equilibrium system, due to the Bohr-van Leeuwen theorem [3,4]. The subtle interplay of chirality ($\Omega \neq 0$) and being out of equilibrium ($\tau_p \neq 0$) is essential for the crystallization. We verify this prediction by simulating the system over a wide range of $R = v_0/\Omega$ and τ_p. Figures 4(a) and 4(c) show the phase diagram in the parameter space of $1/\tau_p$ and R at $\varphi = 0.40$ and 0.35, respectively. The largest values of τ_p explored are 200 for $\varphi = 0.40$ and 10^3 for $\varphi = 0.35$, beyond which preparing stationary states becomes prohibitively difficult. The color of the dots in the phase diagrams represents the average of the hexatic order parameter defined as $\Psi_6 = N^{-1}\langle\sum_{i=1}^{N} \psi_6^i\rangle$, where $\psi_6^i = N_i^{-1}\sum_j e^{6i\theta_{ij}}$ is the local order parameter of the ith particles. The summation is taken over the N_i nearest neighbors of the ith particle and θ_{ij} is the relative angle of the bond between the center of the circular orbit of the particle and that of its nearest neighbors. The figures clearly demonstrate the main features discussed above: the solid phase in the finite range of R confined by the upper and lower bounds of the binary lines, which eventually terminate at a small but finite τ_p. Interestingly, the approxi-

mate locations of the lower and upper phase boundaries, R_l and R_u, can be estimated by purely geometric argument. The lower boundary is estimated by equating the effective packing fraction of circulating particles, $\varphi_{\text{eff}} = \rho\pi R_{\text{eff}}^2$ (where ρ is the number density), to the melting point of a hard-disk system, $\varphi_c \approx 0.7$ [27], which leads

$$R_l = \frac{\sigma}{2}\left(\sqrt{\frac{\varphi_c}{\varphi}} - 1\right) \approx 0.16\sigma \tag{4}$$

for $\varphi = 0.4$. Similarly, the upper boundary can be estimated to be $R_u \approx 0.25\sigma$ using the same equation by replacing φ_c with the maximum hexatic packing $\varphi_m = \pi/(2\sqrt{3}) \approx 0.9$, assuming that particle collisions that would inevitably occur lead to the breakdown of the hexatic order beyond this density. These rough estimates are shown by the arrows in Figs. 4(a) and 4(c), supporting our argument. For more quantitative discussion, an analysis based on the microscopic configurations would be required, which we leave for future work. Note that the upper boundary R_u is significantly lower than the phase boundary of the absorbing phase transition observed in the noiseless limit of $\tau_p = \infty$ at $R \approx 1$ and $\varphi = 0.4$ [19]. This indicates the possible existence of a phase with configurational correlations or with dynamical inhomogeneities between the active phase and the purely absorbing phase. Recalling that the present system is two dimensional, the next concern is the nature of the fluid-solid transition that we are observing. On the one hand, it is well established that the two-dimensional equilibrium fluids of particles with short-range interactions undergo a two-step transition from the fluid phase to the hexatic phase to the solid phase [33–44]. This scenario has also been verified in several active matter models, though the exponents characterizing the transition may differ [45,46]. Conversely, a recent study by Kuroda *et al.* claimed otherwise for out-of-equilibrium systems and demonstrated that the Mermin-Wagner fluctuations are strongly suppressed in cABP due to hyperuniformity at high densities and in the large τ_p regime [22]. To determine which scenario applies to our system, we carefully examine the dependence of the order parameters and their fluctuations. Figure 4(b) shows the slice of the phase diagram at $\tau_p = 10^2$ and $\varphi = 0.4$, displaying the R dependence of the modulus of the global hexatic order parameter $|\Psi_6|$. Figure 4(d) shows the same for $\varphi = 0.35$. Two transitions are clearly observed but they are distinct. At the first transition from a fluid to a hexatic phase around $R \approx 0.15$, $|\Psi_6|$ sharply yet continuously increases, whereas $|\Psi_6|$ drops discontinuously at the second and re-entrant transition to a fluid phase around $R \approx 0.3$. To characterize these transitions, we evaluate the two correlation functions. The first is the translational correlation function of the center of the circular orbit, which is defined by

$$g_0(\boldsymbol{r}) \equiv \frac{1}{\rho N}\left\langle \sum_{i,j} \delta\left(\boldsymbol{r} - \boldsymbol{r}_{ij}^0\right)\right\rangle, \tag{5}$$

where $\boldsymbol{r}_{ij}^0 = \boldsymbol{r}_i^0 - \boldsymbol{r}_j^0$ and $\boldsymbol{r}_i^0$ is the instantaneous position of the center of the circular orbit of the ith particle. Employing the centers of the circular orbits enhances the resolution of the correlations. The second is the orientational correlation

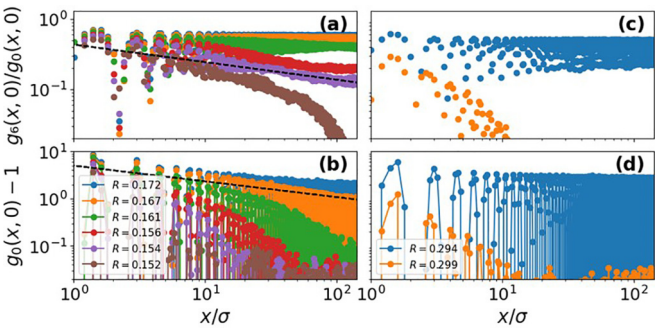

FIG. 5. (a) $g_6(\boldsymbol{r})/g_0(\boldsymbol{r})$ and (b) $g_0(\boldsymbol{r}) - 1$ (bottom) along the direction of $y = 0$ for several R values near the first transition. (c), (d) Same as panels (a) and (b), but for R near the second transition. The dashed lines in panels (a) and (b) represent the power laws $x^{-1/4}$ and $x^{-1/3}$, respectively.

function defined by

$$g_6(\boldsymbol{r}) \equiv \frac{1}{\rho N}\left\langle \sum_{i,j} \psi_6^i \psi_6^{j*} \delta\left(\boldsymbol{r} - \boldsymbol{r}_{ij}^0\right)\right\rangle. \tag{6}$$

Figures 5(a) and 5(b) present one-dimensional cuts of the normalized orientational correlation $g_6(x,0)/g_0(x,0)$ and $g_0(x,0) - 1$ for various R values between 0.152 and 0.172, in the vicinity of the first transition shown in Fig. 4(b). The system size is $N = 40\,824$. The two panels clearly demonstrate the characteristics of two-dimensional solidification predicted by the KTHNY scenario. At the low-R side, the system is in a fluid phase, and both correlation functions decay exponentially. As R increases, $g_6(x,0)$ first exhibits the algebraic decay $\sim x^{-\eta_6}$. The smallest R at which the power law is observed over the entire range of the windows of x is $R_{\text{Hex}} \approx 0.154$ and the power law there is well fitted by using the exponent $\eta_6 = 1/4$. This is the indication that the system undergoes the hexatic transition at R_{Hex}. We also calculate the order parameter Ψ_6 for various system sizes N. We find that $|\Psi_6|$ decays as $N^{-1/2}$ for $R < R_{\text{Hex}}$, a trivial N dependence predicted for systems with short-ranged order. As expected for the quasi-long-range ordered systems, $|\Psi_6| \sim N^{-\eta_6/4}$ at $R = R_{\text{Hex}}$ (see the Supplemental Material [26]). As R increases further, η_6 decreases and the N dependence of $|\Psi_6|$ becomes weaker. Concomitantly, the translational correlation function $g_0(x,0) - 1$ begins to develop a power law $\sim x^{-\eta_G}$. The value at which the power law is seen over the entire range of the windows of x is $R_G \approx 0.162$, which is slightly larger than R_{Hex}. The corresponding exponent is close to $\eta_G = 1/3$ as shown by the dotted line in panel (b) and thus we conclude that R_G marks the hexatic-solid transition. At larger R, η_G keeps decreasing below 1/3. We also calculate the translational order parameter defined by $\rho_G = N^{-1}\langle\sum_{j=1}^N e^{i\boldsymbol{G}\cdot\boldsymbol{r}_j^0}\rangle$, where $\boldsymbol{G}$ is the reciprocal lattice vector obtained from $S(\boldsymbol{q})$ in Fig. 2(b) [47]. We find that $|\rho_G| \sim N^{-1/2}$ for $R < R_G$ and $\sim N^{-\eta_G/4}$ at $R = R_G$ [26]. For $R > R_G$, we find that $g_6(x,0)$ develops a plateau, while $g_0(x,0) - 1$ continues to decay as $\sim r^{-\eta_G}$ where $\eta_G < 1/3$ and decreases with R. Similarly, $|\rho_G|$ also decays as $N^{-\eta_G/4}$ with the same exponent as that of $g_0(x,0) - 1$ [26]. These results suggest that the transition of circularly rotating particles from a fluid to a hexatic crystal transition is two-step:

The first is from the fluid phase to the hexatic phase in which the orientational order becomes quasi long range, whereas the translational order is short-ranged. The second is from the hexatic to the solid phase, in which the orientational order becomes true long-ranged and the translational order becomes quasi long range. This is the same as the two-dimensional melting scenario in equilibrium systems [33–35,37]. We note that the nature of the transition that we observed at moderate densities and with finite τ_p in this study is distinct from that at high densities and the large τ_p limit, where the system develops the genuine long-range translational order and the crystal phase is highly stable [22]. Finally, let us turn our attention to the re-entrant transition near R_u. As shown in Fig. 4(c) and in the Supplemental Material [26], both $|\Psi_6|$ and $|\rho_G|$ drop discontinuously around $R \approx 0.28$. Figures 5(c) and 5(d) show that neither $g_0(x,0) - 1$ nor $g_6(x,0)$ exhibit a sign of algebraic decay. Of course, one cannot exclude the possibility that the continuous and two-step transitions occur within an extremely narrow range of R values. However, we should not be surprised even if the transition is discontinuous. If R exceeds R_u defined by the maximum packing fraction of the effective particles, the orbiting particles will inevitably collide. This collision destroys the circulating orbit and, consequently, the effective particle picture no longer works (see the video in the Supplemental Material [26]). This does not contradict the KTHNY scenario that does not consider the drastic changes to the internal degrees of freedom of the constituents (in this case, the destruction of circular orbits).

IV. SUMMARY

In this article, we have demonstrated the crystallization of the orbiting active particles in two dimensions at low densities. This is only possible if the system breaks the detailed balance of fluctuations and the chiral symmetry simultaneously. The nature of the transitions at least at near R_l, or on the high-Ω side, is akin to an equilibrium two-step transition described by the KTHNY scenario. This scenario is consistent with the equilibrium systems of particles interacting with a soft potential [48]. The next logical question concerns the fate of this transition line at large densities. If both the density and τ_p are large enough, the scenario is completely different, and the hyperuniformity and packing effects stabilize the crystal [22]. Finally, we note that the largest system size of $N = 40\,824$ explored in this study is still moderate for determining whether the fluid-hexatic transition is continuous or not, as corroborated by the large-scale simulations of monatomic equilibrium systems [27,48]. A more elaborate and systematic analysis using the larger systems is left for future work.

ACKNOWLEDGMENTS

We thank Yoshihiko Nishikawa and Harukuni Ikeda for their insightful comments and fruitful discussion. This work was supported by JSPS KAKENHI (Grants No. JP20H00128, No. JP22H04472, No. JP23H04503, No. JP23KJ1068, No. JP24H00192, and No. JP24H02203), AMED Moonshot Program (Grant No. JP22zf0127009), Takeda Science Foundation, and the JST FOREST Program (Grant No. JPMJFR212T).

DATA AVAILABILITY

The data that support the findings of this article are not publicly available. The data are available from the authors upon reasonable request.

[1] L. D. Landau and E. M. Lifshitz, *Statistical Physics* (Pergamon, New York, 1968).
[2] R. Kubo, *Statistical Physics* (North Holland, Amsterdam, 1990).
[3] N. Bohr, *Studier Over Metallernes Elektrontheori* (University of Copenhagen, Copenhagen, 1911).
[4] H. J. van Leeuwen, Problèmes de la théorie électronique du magnétisme, J. Phys. Radium **2**, 361 (1921).
[5] B. Liebchen and D. Levis, Chiral active matter, Europhys. Lett. **139**, 67001 (2022).
[6] E. Lauga, W. R. DiLuzio, G. M. Whitesides, and H. A. Stone, Swimming in circles: Motion of bacteria near solid boundaries, Biophys. J. **90**, 400 (2006).
[7] I. H. Riedel, K. Kruse, and J. Howard, A self-organized vortex array of hydrodynamically entrained sperm cells, Science **309**, 300 (2005).
[8] M. Huang, W. Hu, S. Yang, Q.-X. Liu, and H. P. Zhang, Circular swimming motility and disordered hyperuniform state in an algae system, Proc. Natl. Acad. Sci. USA **118**, e2100493118 (2021).
[9] F. Kümmel, B. ten Hagen, R. Wittkowski, I. Buttinoni, R. Eichhorn, G. Volpe, H. Löwen, and C. Bechinger, Circular motion of asymmetric self-propelling particles, Phys. Rev. Lett. **110**, 198302 (2013).
[10] H. Zhang, K. Qiao, and Y. Han, Power laws in pressure-induced structural change of glasses, Nat. Commun. **11**, 2005 (2020).
[11] D. Banerjee, A. Souslov, A. G. Abanov, and V. Vitelli, Odd viscosity in chiral active fluids, Nat. Commun. **8**, 1573 (2017).
[12] A. P. Petroff, X.-L. Wu, and A. Libchaber, Fast-moving bacteria self-organize into active two-dimensional crystals of rotating cells, Phys. Rev. Lett. **114**, 158102 (2015).
[13] T. H. Tan, A. Mietke, J. Li, Y. Chen, H. Higinbotham, P. J. Foster, S. Gokhale, J. Dunkel, and N. Fakhri, Odd dynamics of living chiral crystals, Nature (London) **607**, 287 (2022).
[14] E. S. Bililign, F. Balboa Usabiaga, Y. A. Ganan, A. Poncet, V. Soni, S. Magkiriadou, M. J. Shelley, D. Bartolo, and W. T. M. Irvine, Motile dislocations knead odd crystals into whorls, Nat. Phys. **18**, 212 (2022).
[15] C. B. Caporusso, G. Gonnella, and D. Levis, Phase coexistence and edge currents in the chiral Lennard-Jones fluid, Phys. Rev. Lett. **132**, 168201 (2024).
[16] V. E. Debets, H. Löwen, and L. M. C. Janssen, Glassy dynamics in chiral fluids, Phys. Rev. Lett. **130**, 058201 (2023).
[17] P. Arora, S. Sadhukhan, S. K. Nandi, D. Bi, A. K. Sood, and R. Ganapathy, A shape-driven reentrant jamming transition in confluent monolayers of synthetic cell-mimics, Nat. Commun. **15**, 5645 (2024).

[18] Z. Ma, Q.-l. Lei, and R. Ni, Driving dynamic colloidal assembly using eccentric self-propelled colloids, Soft Matter **13**, 8940 (2017).
[19] Q.-L. Lei, M. P. Ciamarra, and R. Ni, Nonequilibrium strongly hyperuniform fluids of circle active particles with large local density fluctuations, Sci. Adv. **5**, eaau7423 (2019).
[20] S. Torquato, Hyperuniform states of matter, Phys. Rep. **745**, 1 (2018).
[21] M. Henkel, H. Hinrichsen, and S. Lübeck, *Non-Equilibrium Phase Transitions: Absorbing Phase Transitions* (Springer, Dordrecht, 2008), Vol. 1.
[22] Y. Kuroda, T. Kawasaki, and K. Miyazaki, Long-range translational order and hyperuniformity in two-dimensional chiral active crystal, Phys. Rev. Res. **7**, L012048 (2025).
[23] N. D. Mermin, Crystalline order in two dimensions, Phys. Rev. **176**, 250 (1968).
[24] R. Hanai, Nonreciprocal frustration: Time crystalline order-by-disorder phenomenon and a spin-glass-like state, Phys. Rev. X **14**, 011029 (2024).
[25] M. Kardar, *Statistical Physics of Fields* (Cambridge University Press, Cambridge, 2007).
[26] See Supplemental Material at http://link.aps.org/supplemental/10.1103/yntx-ss9r for details on simulation methods and system-size dependence.
[27] E. P. Bernard and W. Krauth, Two-step melting in two dimensions: First-order liquid-hexatic transition, Phys. Rev. Lett. **107**, 155704 (2011).
[28] Z. Ma and R. Ni, Dynamical clustering interrupts motility-induced phase separation in chiral active Brownian particles, J. Chem. Phys. **156**, 021102 (2022).
[29] A. Onuki, *Phase Transition Dynamics* (Cambridge University Press, Cambridge, 2007).
[30] Y. Kuroda, H. Matsuyama, T. Kawasaki, and K. Miyazaki, Anomalous fluctuations in homogeneous fluid phase of active Brownian particles, Phys. Rev. Res. **5**, 013077 (2023).
[31] Y. Kuroda and K. Miyazaki, Microscopic theory for hyperuniformity in two-dimensional chiral active fluid, J. Stat. Mech. (2023) 103203.
[32] I. Guillamón, H. Suderow, A. Fernández-Pacheco, J. Sesé, R. Córdoba, J. M. De Teresa, M. R. Ibarra, and S. Vieira, Direct observation of melting in a two-dimensional superconducting vortex lattice, Nat. Phys. **5**, 651 (2009).
[33] J. M. Kosterlitz and D. J. Thouless, Ordering, metastability and phase transitions in two-dimensional systems, J. Phys. C **6**, 1181 (1973).
[34] B. I. Halperin and D. R. Nelson, Theory of two-dimensional melting, Phys. Rev. Lett. **41**, 121 (1978).
[35] A. P. Young, Melting and the vector Coulomb gas in two dimensions, Phys. Rev. B **19**, 1855 (1979).
[36] K. J. Strandburg, Two-dimensional melting, Rev. Mod. Phys. **60**, 161 (1988).
[37] J. Y. Lee and K. J. Strandburg, First-order melting transition of the hard-disk system, Phys. Rev. B **46**, 11190 (1992).
[38] J. A. Zollweg and G. V. Chester, First-order melting transition of the hard-disk system, Phys. Rev. B **46**, 11186 (1992).
[39] H. Weber, D. Marx, and K. Binder, Melting of two-dimensional solids: A Monte Carlo study, Phys. Rev. B **51**, 14636 (1995).
[40] A. Jaster, The hexatic phase of the two-dimensional hard disks system, Phys. Lett. A **330**, 120 (2004).
[41] C. H. Mak, Finite-size scaling of the hexatic phase in two-dimensional hard disks, Phys. Rev. E **73**, 065104(R) (2006).
[42] K. Zahn, R. Lenke, and G. Maret, Two-stage melting of paramagnetic colloidal crystals in two dimensions, Phys. Rev. Lett. **82**, 2721 (1999).
[43] Y. Peng, Z. Wang, A. M. Alsayed, A. G. Yodh, and Y. Han, Melting of colloidal monolayers with long-range repulsions, Phys. Rev. Lett. **104**, 205703 (2010).
[44] K. Bagchi, H. C. Andersen, and W. Swope, Computer simulation study of the melting transition in two dimensions, Phys. Rev. Lett. **76**, 255 (1996).
[45] X.-q. Shi, F. Cheng, and H. Chaté, Extreme spontaneous deformations of active crystals, Phys. Rev. Lett. **131**, 108301 (2023).
[46] P. Digregorio, D. Levis, A. Suma, L. F. Cugliandolo, G. Gonnella, and I. Pagonabarraga, Full phase diagram of active Brownian disks: From melting to motility-induced phase separation, Phys. Rev. Lett. **121**, 098003 (2018).
[47] Y.-W. Li and M. P. Ciamarra, Accurate determination of the translational correlation function of two-dimensional solids, Phys. Rev. E **100**, 062606 (2019).
[48] S. C. Kapfer and W. Krauth, Two-dimensional melting: From liquid-hexatic coexistence to continuous transitions, Phys. Rev. Lett. **114**, 035702 (2015).